CHEMISTRY OF MATERIALS

ARTICLE

pubs.acs.org/cm

# Means and Limits of Control of the Shell Parameters in Hollow Nanoparticles Obtained by the Kirkendall Effect

Maria Ibáñez, Jiandong Fan, Wenhua Li, Doris Cadavid, Raquel Nafria, Alex Carrete, and Andreu Cabot*

Departament Electronica, Universitat de Barcelona, Marti i Franques 1, 08028, Barcelona, Spain, and Catalonia Energy Research Institute—IREC, Jardí de les Dones de Negre, 1, Planta 2, E-08930, Sant Adrià del Besós, Barcelona, 08930, Spain

**ABSTRACT:** Recently reported synthetic routes for the production of hollow nanoparticles have stimulated significant interest for the possibilities this novel geometry offers. While advantageous properties have been found and innovative applications have been proposed, the development of the full potential of these new nanostructures is still strongly tied to the extent of control that can be accomplished over their characteristics (e.g., composition, size, shell thickness, and nanocrystalline structure). In the present work, we investigate the means and limits of control over these parameters that can be obtained by the Kirkendall effect synthetic route on cadmium chalcogenide nanocrystalline shells. We demonstrate that the selection of the reactants and oxidation conditions allows some extent of control of the nanocrystalline structure and thickness of the shell. However, the tuning range is limited by the intrinsic restrictions of the synthetic procedure and by the dependence of the particle geometry on the same reaction conditions. Thus, we further explore the range of control over the shell parameters that can be accomplished through post-synthesis processes, such as chemical etching and thermal annealing.

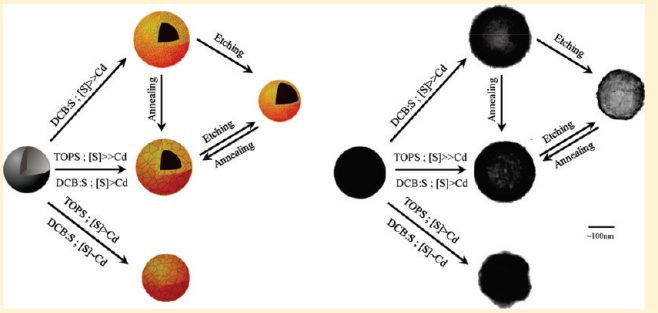


**KEYWORDS:** Nanoparticle, hollow, semiconductor, Kirkendall effect, oxidation

## INTRODUCTION

Many of the advantageous properties of hollow versus solid inorganic nanoparticles result from their lower densities and their larger surface-to-bulk ratio. The reduction of the amount of material decreases both their poisoning effect for *in vivo* applications and their cost for technological uses. At the same time, their large surface-to-bulk ratio offers larger adsorption capabilities and makes them more sensitive to interactions with their surroundings. An additional beneficial property of hollow nanoparticles is their ability to encapsulate other substances within their interior cavity. These qualities make them potentially suitable materials for applications in the fields of catalysis, sensing, and drug delivery.[1,2]

The particular crystallographic arrangement of hollow nanoparticles also provides novel physical properties and potentially improved functionalities.[3−7] As an example, nanocrystalline CdS synthesized into a spherical shell geometry is capable of withstanding extreme stresses and exhibits considerable deformation to failure.[3] As a result of their superior mechanical properties, hollow $WS_2$ nanostructures show outstanding performance as solid-state lubricants.[4] Furthermore, magnetic hollow particles offer extra parameters to tune their magnetic properties,[5] and polycrystalline hollow maghemite nanoparticles show lower blocked-to-superparamagnetic transition temperatures, significant coercivities, and higher irreversibility and magnetic saturation fields than their solid counterparts.[6]

Most of the proposed innovative uses of hollow inorganic nanostructures in the fields of catalysis, sensing, and drug delivery ultimately depend on the accessibility to their internal cavity. The permeability of the shell, which controls such access, is determined by its nanocrystalline structure and thickness. In a similar way, tribological, magnetic, and also optical and piezoelectric properties of hollow nanoparticles, depend on their composition, but also on the geometric parameters of their shells and on their nanocrystalline structure. Therefore, the extent of control over the shell parameters that we can accomplish ultimately determines to what degree we can benefit from the potential advantageous properties of hollow nanostructures.

Since the initial reports,[1,8] the mechanism of formation of hollow nanoparticles via the nanoscale Kirkendall effect has been successfully applied to the synthesis of hollow nanostructures from a large amount of different materials including phosphides, oxides and other chalcogenides, demonstrating the broad applicability of this mechanism.[9] However, the synthesis of hollow nanoparticles by the Kirkendall effect is not without limitations. Hollow nanostructures cannot be obtained from all materials, nor can every particle size, shell thickness, or crystallinity be produced via this route.

In the simplest scenario, the synthesis of colloidal hollow nanostructures by the Kirkendall effect is a one-pot, two-step process. The first step involves the synthesis at temperature T1 of solid particles of at least one of the elements of the final shell (A). In the next step, a second element (B) is reacted with the A

**Received:** March 5, 2011
**Revised:** April 29, 2011
**Published:** May 24, 2011

ACS Publications © 2011 American Chemical Society

**Scheme 1. One-Pot Synthetic Route for the Synthesis of Hollow Particles through the Nanoscale Kirkendall Effect**

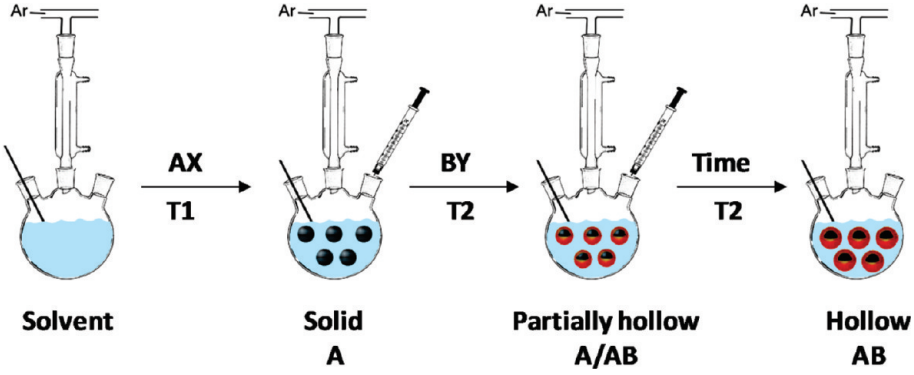


particles at temperature T2 to yield an AB composite (see Scheme 1). Several factors determine the final geometry of AB particles: the relative self-diffusivities of elements A and B in AB, their relative rates of reaction at the A/AB and AB/B interfaces, the size of the initial template A particles, and the change of volume from A to AB. The theoretical limit on the largest inner-to-outer radius ratio ($R_I/R_O$) and thinnest shell of a hollow particle obtained by the Kirkendall effect is reached when the entire shell grows at the composite/solution or AB/B interface. In this limit, and considering no porosity within the shell, $R_I/R_O$ is given by the molar volume ratio between A and AB, which is also known as the Pilling−Bedworth ratio:

$$\frac{R_I}{R_O} = (\theta + 1)^{-1/3} \quad (1)$$

$$\theta \equiv \frac{V_{AB}}{V_A} = \frac{FW_{AB}\rho_A}{\rho_{AB}FW_A} \quad (2)$$

$FW_{AB}$ and $FW_A$ are the formula weights of the composite and template materials, respectively, and $\rho_{AB}$ and $\rho_A$ represent their respective densities. In this limit, the shell thickness is determined by the initial particle diameter and the volume ratios:

$$l = R_O - R_I = R_I\lfloor(\theta + 1)^{1/3} - 1\rfloor \quad (3)$$

An obvious way to control the shell thickness is by tuning the template particle size. All conditions being the same, smaller initial solid particles result in hollow structures with thinner shells. A second evident way to tune the shell thickness is by reacting only partially the solid template particle. While the first procedure does not allow independent control of the shell size and thickness, the second one yields only partially hollow structures with heterogeneous compositions.

In this work, we explore the means and limits of control over the thickness and crystal domain size of nanocrystalline shells obtained through the nanoscale Kirkendall effect. We use the oxidation reaction of Cd particles with chalcogens to investigate these processes. Cadmium chalcogenides, having direct band gaps in the optical region and piezoelectric properties, are materials particularly suited for optical, optoelectronic, and electromechanical applications.[10] Moreover, the very high mobility of Cd at low to moderate temperatures affords synthesis of hollow particles in the 0.1−1 $\mu$m size range. Such large sizes simplify the discrimination of the parameters and mechanisms having a dominant role on their formation.

## EXPERIMENTAL SECTION

Solid cadmium particles were synthesized by injecting dimethylcadmium (0.1 mg, 97%, Strem) with trioctylphosphine (TOP) (1 mL, 97%, Strem) into trioctylphosphine oxide (TOPO) (10 g, 99% Arcos) at 330 °C. In the presence of no oxidizing element, dimethylcadmium decomposes to metal cadmium. At sufficiently high temperatures, cadmium forms spherical droplets in the liquid phase (Cd mp 321 °C), which solidify into spherical Cd particles as the temperature decreases. The size of the cadmium particles can be tuned by the concentration of the injected solution and the solution stirring rate.[12]

To sulfidize the colloidal Cd crystals with molecular sulfur in dichlorobenzene (DCB:S), a 20% sulfur solution was prepared inside the glovebox by mixing elemental sulfur (99.998%, Aldrich) in anhydrous 1,2-dichlorobenzene (99%, Aldrich). Dissolution was carried out using a heated ultrasound sonicator, while keeping the sample closed under air-free conditions inside a vial accessible through a septum. The sulfur solution has a dark-brown color. This solution (0.5−6.7 mL) was injected through a septum into the hot solution containing the Cd crystals. The reaction temperature was set between 200 and 300 °C. After injection, the temperature drops a certain amount, depending on the injected volume, but is quickly raised as part of the injected dichlorobenzene is removed by evaporation. The sulfidation requires anywhere from a few minutes to hours and can be qualitatively monitored from the solution's change in color from gray to orange.

In a similar way, 10% TOP complexes of Te, Se, and S (denoted as TOPTe, TOPSe, and TOPS, respectively) were prepared inside the glovebox by stirring the appropriate amounts of TOP with Te (99.999%, Aldrich), Se (99.999%, Aldrich), and S during 24 h. The TOPTe, TOPSe, and TOPS complexes were injected into the heated Cd solution at temperatures of 200−300 °C to produce CdTe, CdSe, and CdS hollow or solid particles, as described in the text.

To control the shell thickness of CdS hollow particles, an etching process with HCl in chloroform is used. Typically, with a solution of HCl in $CHCl_3$ (0.1 M), a solution of CdS particles ($4 \times 10^{-4}$ M) completely dissolves within ~3 min. The chemical attack is homogeneous at the crystal size scale and can be precisely quenched at any target shell thickness by neutralizing the acid with a weak base such as oleylamine. In this way, the shell thickness can be easily tuned over the reaction time.

The crystal structure of the samples was measured using powder X-ray diffraction (XRD). Such XRD analyses were obtained on a Bruker AXS diffractometer using Co Kα radiation (1.79026 Å) and a general area detector. The instrument resolution was 0.05° in 2$\theta$, and the

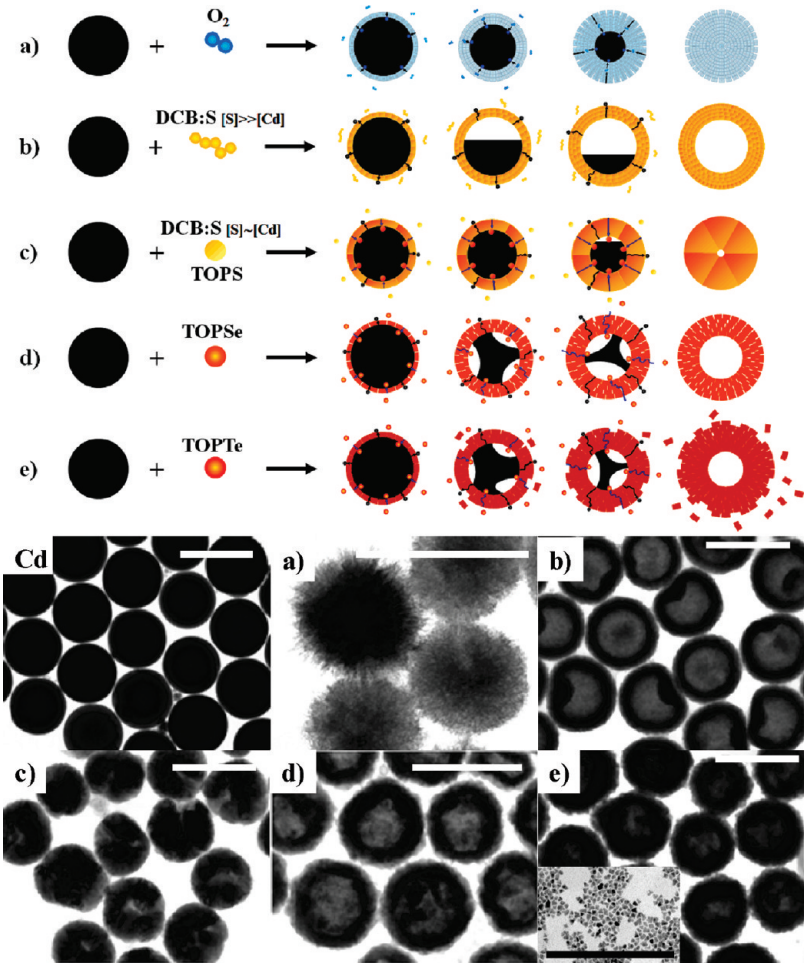


**Figure 1.** Scheme (top) and TEM micrographs (bottom) of the reaction of Cd particles with (a) oxygen, (b) molecular sulfur in solution ([S]/[Cd] = 8), (c) TOPS, (d) TOPSe, and (e) TOPTe. All the scale bars on the TEM micrographs correspond to 500 nm, except for the inset in the image shown in panel e, which corresponds to 100 nm. The TEM micrograph labeled "Cd" corresponds to the initial unoxidized Cd particles.

acquisition time for each sample was ~1 h. XRD samples were prepared in air by depositing the precipitated particles on a quartz substrate.

TEM micrographs were obtained using a Tecnai G2 S-Twin electron microscope (200 kV). TEM samples were prepared by placing a drop of the colloidal solution containing the nanoparticles onto a carbon-coated copper grid at room temperature and ambient atmosphere. Only the grid containing the initial cadmium nanoparticles was prepared and mounted in the TEM holder under an argon atmosphere. This sample was quickly transferred to the TEM, reducing its air exposure to ~20 s.

## RESULTS AND DISCUSSION

Solid cadmium particles were prepared by decomposition of dimethylcadmium in trioctylphosphine oxide at 330 °C. Cd particles obtained following this procedure were spherical but monocrystalline, and their size could be controlled in the range of 0.1−1 $\mu$m.[11,12] The reaction of the colloidal Cd crystals with chalcogens was carried out by injecting the selected chalcogen precursor or bubbling synthetic dry air into/through the heated solution containing them.

**Influence of the Ion Self-Diffusion Coefficients on the Final Morphology.** Urchin-shaped CdO particles with small crystallographic domain sizes of ~7 ± 2 nm were the product of the Cd reaction with oxygen (Figure 1a). No hollow CdO particles could be obtained by reacting the Cd particles with oxygen in the conditions and temperature range tested (200−320 °C). To the best of our knowledge, there are no reported data of the oxygen solubility in TOPO, which may be relatively low. In such a case, bubbling synthetic air inside the solution would introduce a limited concentration of oxygen in the solvent. While the oxygen concentration in solution was unknown, the moderate reaction times needed for the oxidation reaction to be complete point toward a diffusion-limited shell growth. The failure to obtain hollow CdO particles by the nanoscale Kirkendall effect indicates a faster diffusion of oxygen than cadmium through the CdO shell or a preferential reaction at the Cd/CdO interface. The urchin shape of the CdO particles is associated with the volume expansion obtained from the reaction of Cd with O to form CdO. This volume expansion at the Cd/CdO interface pushes out the preformed CdO. Because of the surface curvature of the spherical particles, when expanding, the external oxide layer accumulates a tensile stress that leads to their fracture. These shell fractures provide avenues for oxygen transport in solution, which maintain a fast reaction rate, resulting in the formation of small crystallographic domains over the entire oxidation process.

In contrast, the reaction of Cd particles with a large excess of molecular sulfur in dichlorobenzene (DCB:S) resulted in


dx.doi.org/10.1021/cm2006633 |*Chem. Mater.* 2011, 23, 3095–3104

**Table 1. Pilling−Bedworth Ratio ($\theta$), Theoretical Maximum $R_I/R_O$ Ratio for the Reaction of Cadmium with Chalcogenides, and Self-Diffusion Coefficients ($D = D_0 \exp[-E/(kT)]$) of the Ions in the Corresponding Cadmium Chalcogenide[13]**

| | | | Cation | | Anion | |
|---|---|---|---|---|---|---|
| | $\theta$ | $R_I/R_O$ | $D_0$ [m$^2$/s] | $E$ [eV] | $D_0$ [m$^2$/s] | $E$ [eV] |
| CdTe[a,b] | 2.98 | 0.63 | $1 \times 10^{-4}$−$3 \times 10^{-2}$ | 2.1−2.7 | $2 \times 10^{-8}$−$8 \times 10^{-11}$ | 1.4 |
| CdSe[b,c] | 2.53 | 0.66 | $2 \times 10^{-7}$−$9 \times 10^{-6}$ | 1.3−2.7 | $3 \times 10^{-7}$−$9 \times 10^{-7}$ | 1.3−1.6 |
| CdS[d,e] | 2.30 | 0.67 | $3 \times 10^{-6}$−$7 \times 10^{-2}$ | 1.9−2.7 | $1.6 \times 10^{-6}$ | 2.1 |
| CdO[f,g] | 1.21 | 0.77 | | | $4 \times 10^{1}$−$8 \times 10^{2}$ | 4.0 |

[a] Data taken from ref 14. [b] Data taken from ref 15. [c] Data taken from ref 16. [d] Data taken from ref 17. [e] Data taken from ref 18. [f] Data taken from ref 19. [g] Data taken from ref 20.

spherical hollow CdS particles with small crystallographic domains (~8 ± 2 nm) and large inner-to-outer radius ratios: $R_I/R_O \approx 0.65 \pm 0.02$ (see Figure 1b). This is the largest $R_I/R_O$ ratio reported for hollow nanostructures obtained via the Kirkendall effect. The very large $R_I/R_O$ ratio, which is close to the theoretical limit, involves a complete CdS shell growth at the shell/solution interface. Such a localization of the reaction front, coupled to the high sulfur concentration in solution, provide unambiguous evidence of faster cadmium diffusion than sulfur diffusion through the formed CdS shell.

The reaction of Cd particles with large excesses of trioctylphosphine selenide (TOPSe) and with trioctylphosphine telluride (TOPTe) in the temperature range of 200−300 °C resulted in hollow CdSe and CdTe structures, having $R_I/R_O \approx 0.5$ and $R_I/R_O \approx 0.3$, respectively (see Figures 1d and 1e). As a product of the reaction of Cd with TOPTe, a large population of separated CdTe crystallites ~20 nm in diameter was also obtained (see Figure 1e, inset). The moderate $R_I/R_O$ values observed point toward a divided reaction front: While part of the reaction occurs at the chalcogenide/solution interface, pulling cadmium from the core, a partial inner shell growth and possible intergrain reaction also occur.

In Table 1, the Pilling−Bedworth ratio and the maximum theoretical $R_I/R_O$ ratio for the reaction of Cd with chalcogenides and oxygen is displayed. In the same table, the reported ion self-diffusion coefficients in cadmium chalcogenides are summarized. These values were obtained at high temperatures ($T > 500$ °C) from the analysis of macroscopic crystals. Notice that the anion self-diffusion coefficient strongly depends on the element's atomic number. While the activation energy increases with the anion electronegativity (that is, with the ionicity of the chalcogenide bonds), the diffusion constant increases as the anionic radius decreases. In contrast, the reported cation self-diffusion coefficients are fairly uniform for the different chalcogenides. These ion self-diffusion trends suggest faster anion self-diffusion than cation self-diffusion in CdTe and CdSe, and similar self-diffusion coefficients for CdS. Although we have no data on the bulk diffusion of Cd in CdO crystals, the noted trends of the self-diffusion coefficients for the different cadmium chalcogenides, coupled with the experimental observation of slower anion diffusion than cation diffusion in simple oxides,[19] signals a faster diffusion of cadmium than oxygen in CdO. Thus, from a simple extrapolation of the anion and cation self-diffusivity coefficients previously reported and considering a self-diffusion limited shell growth, we would predict the following: (i) the reaction of cadmium with large oxygen concentrations result in thin CdO shells with $R_I/R_O \approx 0.77$, (ii) the reaction of cadmium with large sulfur concentrations to produce hollow structures with small inner-to-outer diameter ratios, and (iii) the reaction of Cd with large Se and Te concentrations to result in solid structures.

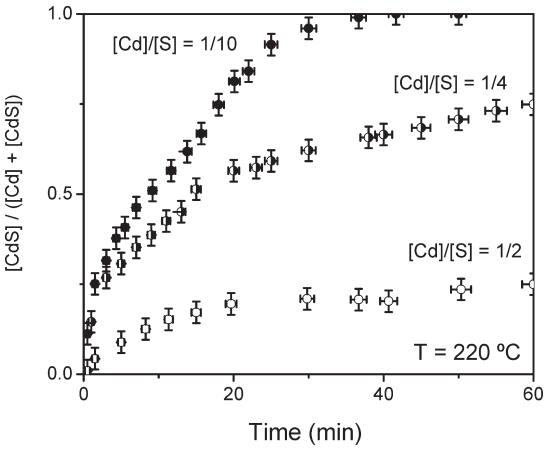


**Figure 2.** Evolution of the CdS formed by reaction of Cd particles with different concentrations of sulfur in solution. The reaction temperature was set at 220 °C.

The experimental results shown here are symptomatic examples of the obvious discrepancies that exist between the morphologies experimentally obtained from the oxidation reaction of metal nanoparticles and the predictions taken from the straightforward extrapolations of the bulk self-diffusion coefficients previously reported. This lack of reliability on the morphology predictions originates from neglecting a possible change of the diffusion mechanism with the temperature, the material crystallinity, or the reactants concentration. The dominant diffusion mechanisms at the relatively low synthesis temperatures used in the present work may differ from those having a main role at the higher temperatures previously employed to evaluate the self-diffusion coefficients. Similarly, the self-diffusivity values previously reported were obtained from the analysis of macroscopic crystals, and thus correspond to lattice self-diffusion coefficients. However, in polycrystalline materials, the self-diffusion coefficients strongly depend on the crystallographic nanostructure. In polycrystalline shells with small crystal domains, the diffusion through grain boundaries is dominant, since grain-boundary diffusivity is generally orders of magnitude larger than that observed through the lattice. Reactants are forced to diffuse through the lattice only in materials with large crystallographic domains. It is only in this case that the bulk diffusivities prevail. Notice, finally, that the concentration of Cd in the inner interface was, in all cases, much larger than the concentration of reactant in solution. It is well-known that the diffusivity mechanism may also

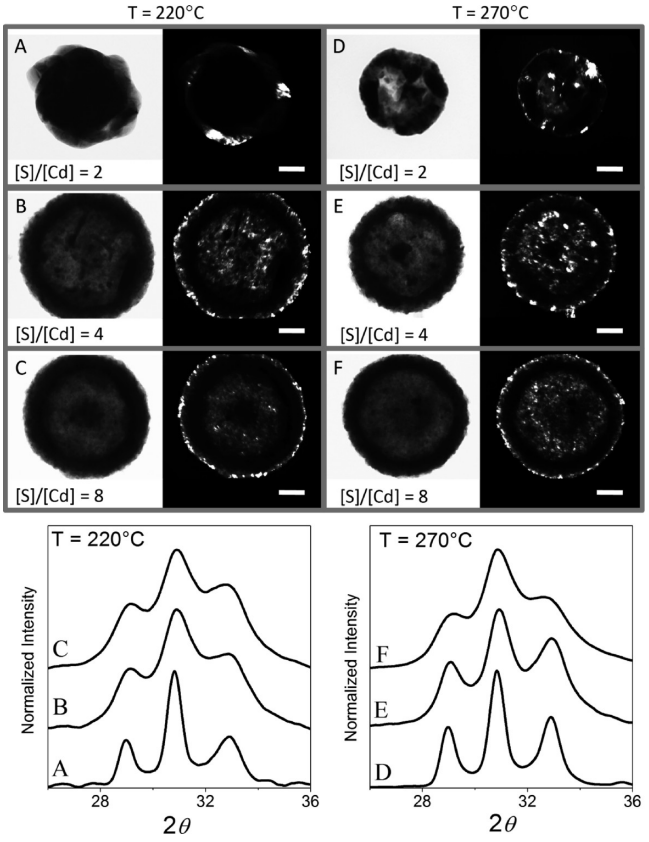


**Figure 3.** Dark-field and bright-field TEM micrographs of CdS particles reacted at two different temperatures with increasing sulfur concentrations. The average crystallite domain size (CDS) is obtained from the TEM micrographs and the XRD data using the Debye−Scherrer equation: (A) 220 °C, [S]/[Cd] = 2, CDS ≈ 100 nm, $R_I/R_O$ = 0, incomplete reaction; (B) 220 °C, [S]/[Cd] = 4, CDS = 14 nm, $R_I/R_O$ = 0.65; (C) 220 °C, [S]/[Cd] = 8, CDS = 8 nm, $R_I/R_O$ = 0.64; (D) 270 °C, [S]/[Cd] = 2, CDS ≈ 100 nm, $R_I/R_O$ = 0.48; (E) 270 °C, [S]/[Cd] = 4, CDS = 26 nm, $R_I/R_O$ = 0.65; (F) 270 °C, [S]/[Cd] = 8, CDS = 9 nm, $R_I/R_O$ = 0.66. Scale bar corresponds to 100 nm.

depend on the concentration of the diffusing elements, especially in the particular case of self-diffusion, where the diffusing species control the concentration of vacancies on the crystal structure.

**Influence of the Precursor Concentration.** Except in very particular cases,[21] the shell curvature and the lattice mismatch between the template and the shell compounds inevitably result in polycrystalline shells. The rates of nucleation and crystallite growth control the shell nanocrystalline structure. These rates are determined by the concentration of precursor in solution, the nature of the reactants, and the temperature.

We investigate the influence of the precursor concentration on the nanocrystalline structure of the resulting shell by reacting Cd particles with different concentrations of DCB:S to yield CdS. The rate of these reactions was measured by analyzing aliquots removed at successive times after the sulfur injection. The appearance of CdS and the concomitant decrease in metal Cd, as a function of time, was quantitatively followed using X-ray diffraction (see Figure 2).

In a previous publication, we showed that, when reacting Cd particles with a large excess of sulfur in solution, the reaction rate is limited by the diffusivity of Cd through the shell.[17] We further concluded that, in the temperature range tested (200−300 °C),

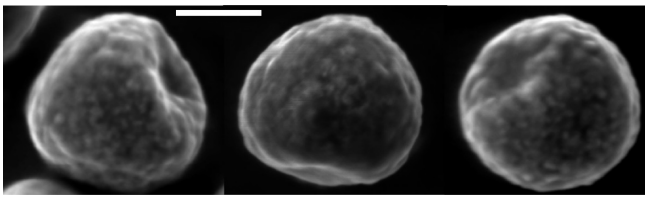

**Figure 4.** SEM micrograph of CdS particles clearly showing visible buckles. Scale bar corresponds to 200 nm.

the Cd diffusion takes place through the CdS grain boundaries. In this regime, each Cd ion reaching the CdS/solution interface ($\geq 10^4$ atoms/s) immediately reacts with sulfur. This fast reaction rate of the Cd atoms reaching the CdS/solution interface leads to a high frequency of nucleation events, accounting for small crystallite sizes and an overall preserved spherical geometry. The average crystallographic domain size within the shell, estimated from both dark-field transmission electron microscopy (TEM) micrographs and the linewidths of the X-ray diffraction (XRD) peaks using the Scherrer equation, is typically $\sim 8 \pm 2$ nm (see Figure 3). In such fine polycrystalline shells, considerable buckling is observed (see Figures 1b and 4). Buckles are formed during the early stages of particle sulfidation. When the CdS polycrystalline shell is very thin, the Cd outward diffusion is not compensated by an inward flow of vacancies or solution, but by an inward curvature of the shell following the asymmetric cadmium core shrinkage. As the shells thickness increases, it gains rigidity, up to a point where it can support the pressure gradient created by the inward flow of vacancies without further buckling. At this stage, vacancies accumulate at the Cd/CdS interface, while solution molecules may also start to flow inside the shell through the grain boundaries. Thus, a decohesion of the shell from the metal core is obtained.

For lower nominal sulfur concentrations ([S]/[Cd] < 6), the sulfur content in solution becomes the reaction-rate-limiting parameter and the reaction proceeds at a slower rate ($\leq 1 \times 10^4$ s$^{-1}$). At these lower S-impeding rates, Cd accumulates on the surface of the preformed CdS crystallites, promoting crystal growth over nucleation of new crystallites at the Cd surface. Thus, larger crystallographic domains, up to 100 nm, result (see Figure 3). Concomitant with an increase of the crystallographic domain size, a clear reduction of $R_I/R_O$ is noticed at relatively low sulfur concentrations ([S]/[Cd] ≤ 2) (see Figure 3). Such a reduction of $R_I/R_O$ denotes some extent of inward growth of the shell, which we associate with a change of the shell growth regime, from self-diffusion to reaction-controlled. That is, the combination of slow shell growth due to a low precursor concentration in solution, and the relatively low DCB:S reaction probability ($\sim 10^{-3}$) allows sulfur to diffuse across the slow-growing shell and react simultaneously at both interfaces. Figure 5a shows the dependence of $R_I/R_O$ on the sulfur impingement rate obtained from a simple kinetic model of the shell growth.[22] Fixing the concentration of Cd particles, the approximated sulfur concentration needed to reach a given impingement rate was calculated and is also shown in Figure 5a. For this calculation, a Stokes−Einstein relation was used to estimate the sulfur diffusivity. Notice that, at a fixed [S]/[Cd], lower impingement rates could be also obtained by reducing the concentration of both Cd and S in solution, increasing the solvent viscosity or increasing the size of the sulfur precursor. The evolution of $R_I$ and $R_O$ for three different sulfur


dx.doi.org/10.1021/cm2006633 |Chem. Mater. 2011, 23, 3095–3104

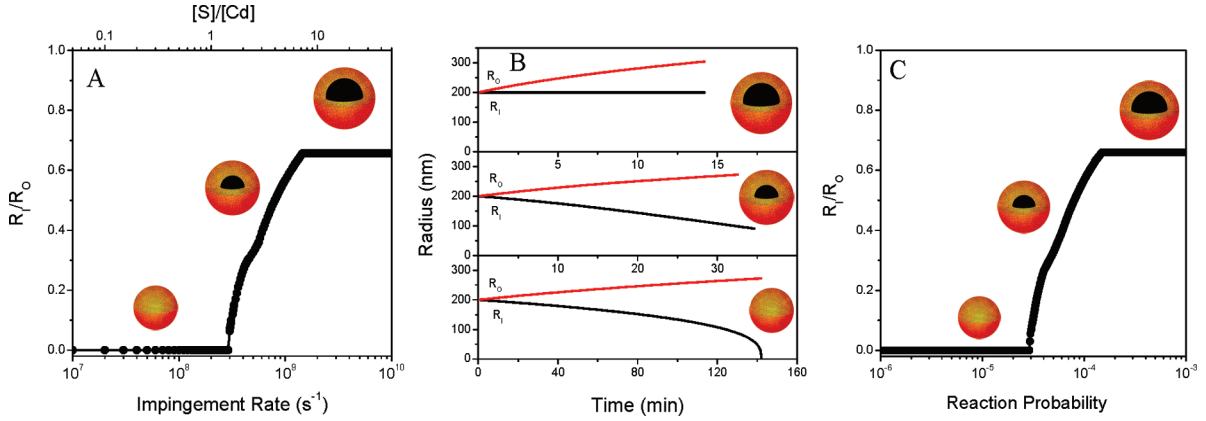


**Figure 5.** Simulation of the inner-to-outer radius ratio obtained from the reaction of 400-nm Cd with sulfur: (a) dependence of the radius ratio on the impingement rate and sulfur concentration in solution; (b) time evolution of the inner and outer radii at three different sulfur concentrations ([S]/[Cd] = 9.5 (top), [S]/[Cd] = 2.5 (middle), and [S]/[Cd] = 0.5 (bottom)); and (c) dependence of the radius ratio on the precursor reactivity.

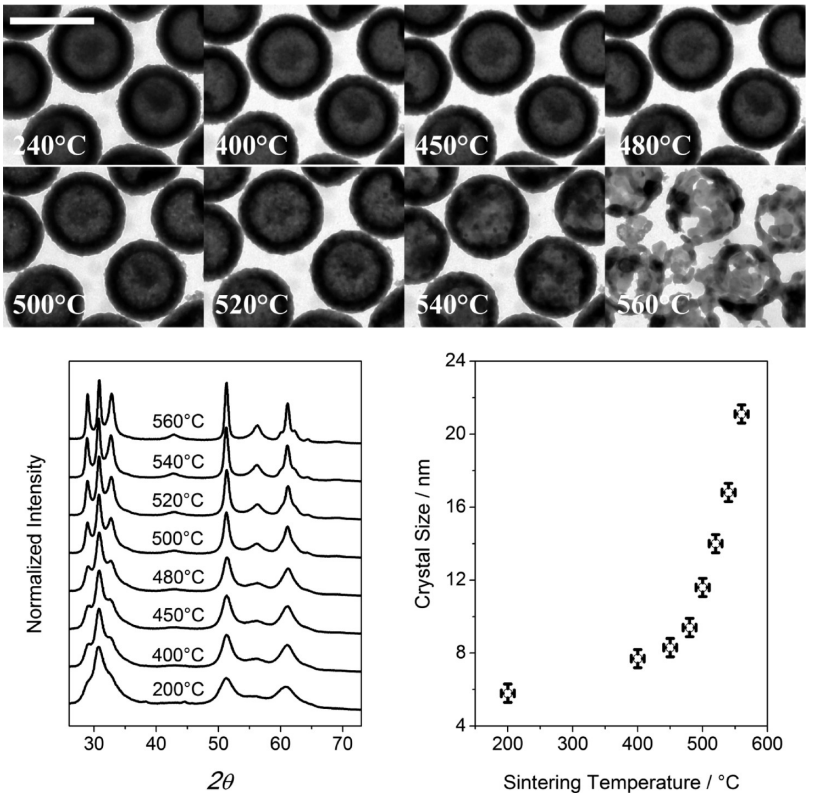


**Figure 6.** TEM micrograph, XRD spectra, and graph of the average crystal domain size of the particles obtained after sintering at different temperatures, from 400 °C to 560 °C. The original material and XRD spectra is also shown as sintered at 240 °C, which corresponds to the synthesis temperature. Scale bar = 500 nm.

concentrations obtained from the same kinetic model is shown in Figure 5b. Obviously, a value of [S]/[Cd] ≤ 1 would not lead to completely oxidized CdS particles but, rather, core−shell heterostructures. Furthermore, in our experimental setup, the combination of a low synthesis temperature (≤220 °C) and a low sulfur concentration in solution ([S]/[Cd] ≤ 2) does not allow the reaction to proceed to completion, because of the loss of sulfur by evaporation during the long reaction time. Under these conditions, the final product of the reaction of Cd with low concentrations of DCB:S are Cd/CdS core−shell structures without detachment or void formation at the interface (see Figure 3a).

**Influence of the Precursor Reactivity.** To exemplify the effect of the precursor reactivity, Cd particles were reacted with relatively large concentrations of trioctylphosphine sulfide (TOPS). The phosphine-sulfur complex is a more stable sulfur source than the molecular sulfur dissolved in DCB. At the same time, the larger TOPS molecules have associated a lower diffusivity in solution and, thus, a lower impingement rate than DCB:S at the same concentration.


dx.doi.org/10.1021/cm2006633 |*Chem. Mater.* 2011, 23, 3095–3104

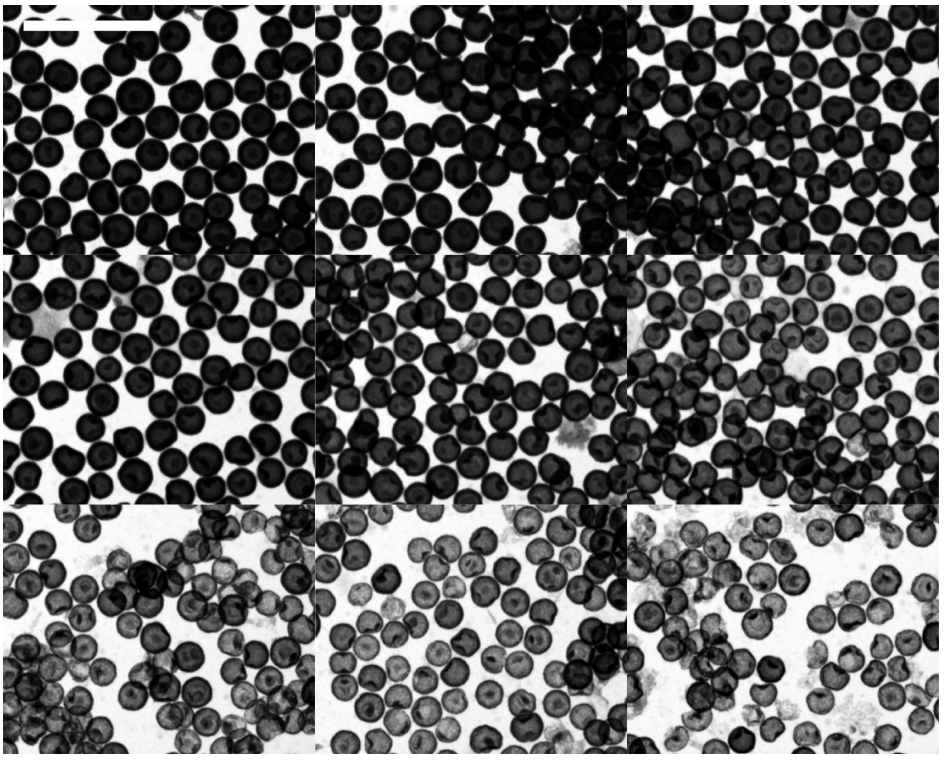

**Figure 7.** TEM micrograph of CdS particles etched with HCl for increasing time intervals (10-s steps). Scale bar = 2 $\mu$m.

The reaction of 0.1 M Cd with 0.6 M of TOPS at $T < 300$ °C proceeds at a slow rate ($\leq 1 \times 10^3$ atoms/s) and results in solid or nearly solid CdS particles (Figure 1c). In the same way as when the DCB:S concentration was reduced, it is experimentally observed that the low reaction rates associated with the sulfidation of Cd particles with relatively larger concentrations of a less-reactive sulfur source promote the crystallite growth over the nucleation rate and results in shells with large crystallographic domain sizes (~100 nm). Again, the obtained increase of the crystallographic domains with TOPS is concomitant with a decrease of the $R_I/R_O$ (Figure 1c). From a synthetic point of view, it is interesting to note that, in contrast to the reaction of molecular sulfur dissolved in DCB, the use of TOPS prevents the vaporization of sulfur, allowing the synthesis of solid CdS particles from the complete sulfidation of Cd cores.

In an analogous case than when reacting Cd particles with low concentrations of DCB:S, we consider the reaction of Cd particles with relatively larger concentrations of TOPS to take place in a reaction-limited regime. In this case, the limiting reaction rate factor may not be the impingement rate but the reaction probability of the TOPS precursor with Cd. In Figure 5c, the dependence of $R_I/R_O$ on the reaction probability is plotted. A decrease in the reaction probability allows a homogeneous distribution of sulfur across the shell, habilitating the Cd−S reaction to occur at both interfaces simultaneously.[22] Note that both reduced sulfur precursor reactivities and reduced impingement rates result in similar decreases of $R_I/R_O$. Because TOPS has a higher stability than DCB:S, but also a lower diffusivity and, thus, a lower impingement rate for the same concentration, both factors will influence in the same direction in the observed decrease of $R_I/R_O$ at higher concentrations than when reacting Cd particles with DCB:S.

We further speculate that the larger CdS crystallographic domains obtained both, when reducing the sulfur concentration or its reactivity, may also have a direct influence on the concomitant decrease of $R_I/R_O$. While intercrystal diffusion is considered to be the main mechanism of Cd transport through fine polycrystalline shells,[11] the formation of large crystallographic domains increases the weight of lattice over surface diffusion. Previous studies showed that, at high temperatures, the Cd lattice diffusion is slightly faster than that of sulfur in CdS.[18] However, at moderate temperatures ($T < 600$ °C), Cd lattice diffusion was observed to decrease when increasing the Cd partial pressure, which points toward a diffusion mechanism controlled by Cd vacancies.[23] In this scenario, the large excess of cadmium in each partially reacted particle may significantly reduce the concentration of Cd vacancies inside the crystals. In the same direction, the reduction of the sulfur concentration in solution or the use of a more-stable sulfur source may increase the concentration of S vacancies in the structure, allowing a faster S lattice diffusion. Therefore, the growth of the crystallographic domains associated with a decrease of the nucleation-versus-growth rates with the decrease of the sulfur concentration or reactivity may have an associated progressive shift of the dominant Cd and S self-diffusion mechanism. This shift could reverse the ratio between the Cd and S self-diffusivities and therefore modify the geometry of the obtained particles.

On the other hand, more-reactive precursors avoid the oxidation reaction of Cd particles to fall into a reaction-rate-limited regime. When reacting Cd with different concentrations of TOPTe, hollow particles with small $R_I/R_O$ and a simultaneous large population of independent 20-nm CdTe crystals is consistently obtained (see Figure 1e). Because of the high thermodynamic driving force for CdTe formation, the reaction of the Cd particles with TOPTe is very fast (~$3 \times 10^6$ atoms/s with

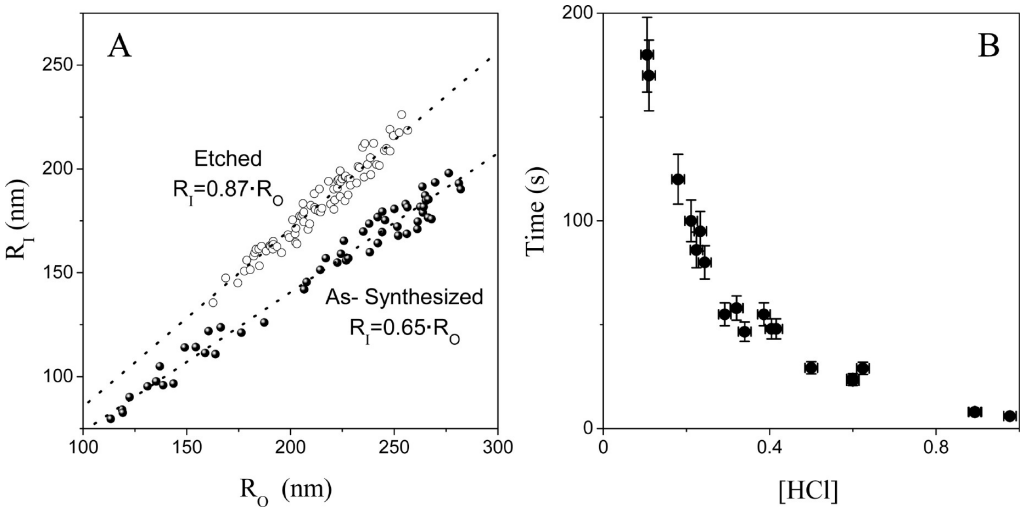


**Figure 8.** (A) Dependence of the particle interior radius on the particle external radius for different CdS particles before and after etching with HCl for 30 s. (B) Time required for the complete dissolution of the CdS shells in HCl, as a function of the acid concentration.

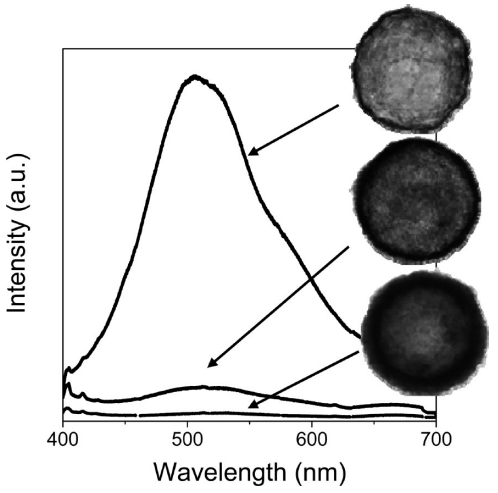


**Figure 9.** Photoluminescence spectra of the original CdS hollow particles (average shell thickness of ~60 nm) and that of two samples having thinner shells (average shell thicknesses of ~30 and ~14 nm) obtained by etching. The particle density is similar for the three samples.

[TOPTe] = 2 × [Cd] ≈ 0.2 M). This rapid shell growth, coupled with the large volume expansion from Cd to CdTe ($\theta$ = 2.98), and the probable intergrain reaction, develops large tensile stresses that are relieved by the partial cracking and delamination of the CdTe shell. The shell porosity retrofits a fast reactant transport by providing efficient paths for ion diffusion and transport of TOPTe in solution, maintaining a fast reaction rate through the entire process. At the same time, the efficient TOPTe transport through the cracks expands the reaction front to the Cd/CdTe interface and the intergrain reaction.

**Post-Synthesis Processing.** The experimental results shown here indicate that the precursor reactivity and concentration not only influence the nanocrystalline structure of the formed compound, but they also determine the shell growth regime and, thus, the final particle morphology. Such correlation between the particle geometry and its nanocrystalline structure constrains the range of crystal domain sizes and shell thicknesses available for hollow structures obtained by means of the Kirkendall effect. At the same time, an intrinsic lower limit of the shell thickness exists, which depends on the particle size and composition.

In order to extend the range of geometric parameters and shell crystallinity available for hollow particles obtained by the Kirkendall effect synthetic route, post-synthesis processes, such as sintering and etching of the particles, can be used.

**Thermal Annealing.** A TEM micrograph of the same particles after undergoing successive thermal annealing treatments at temperatures of 450−560 °C are shown in Figure 6. The sintering temperature dependence of the average crystal domain size inside the shell obtained from the fitting of the XRD spectrum, using the Scherrer equation, is shown in the same figure. The sintering processes were conducted for 2 h in an argon atmosphere. Notice that the sintering of the CdS shells is limited by the stresses resulting from the grain growth, which eventually lead to the shell rupture. For the CdS shells investigated here, with average diameters of ~400 nm and shell thicknesses of ~60 nm, we found the limit on the sintering process to be at a temperature of 560 °C. Such a sintering process doubles the mean crystal domain sizes, from 8 nm to ~17 nm. Further crystal domain growth on preformed hollow particles resulted in the appearance of cracks in the shells.

Previous studies concluded that hollow nanoparticles obtained via the Kirkendall effect were unstable.[24] In these previous works, hollow nanostructures were foreseen to collapse to solid particles by an outward diffusion of vacancies, with their lifetime depending on the vacancy diffusivity coefficients and the particle size. The shrinkage of relatively small hollow nanoparticles was experimentally demonstrated previously for different materials.[25] The experimental results shown here demonstrate that, when supplying enough energy for the ions to relocate, relatively large hollow particles do not collapse into solid spheres, but rather, their crystallographic domains sinter, which ultimately results in shell fracture. The large temperatures needed to crack the CdS particles (~550 °C) allow us to consider the hollow nanoparticles studied here to be sufficiently stable for applications at low and moderate temperatures.

**Chemical Etching.** Colloidal CdS shells were etched using a solution of HCl in $CHCl_3$. The HCl etching process allows

modification of the shell thickness with considerable control, as shown in Figures 7 and 8a. The shell thickness reduction can also be monitored *in situ* by the decrease of the optical absorption of the particles in solution. Using a 0.1 M solution of HCl, the total dissolution of a $4 \times 10^{-4}$ M solution of CdS particles takes place within ~3 min (see Figure 8b). Thus, the reaction can be rapidly quenched at any time, for any shell thickness, by introducing an equivalent amount of amine to neutralize the HCl. The chemical attack occurs mostly on the outer surface of the shell and is significantly homogeneous. However, the heterogeneity of the initial shell thickness limits the thinnest complete hollow particle that can be obtained to ~10 nm (see Figure 7). Despite the small crystallite domain size and shell thicknesses, particles do not show efficient band-to-band photoluminescence. When reducing the thickness of the shell, only the fluorescence band associated with transitions involving surface states develops at 600 nm (see Figure 9).

## CONCLUSIONS

Hollow CdS, CdSe, and CdTe particles can be obtained from the reaction of cadmium with the respective chalcogen, signaling faster cation self-diffusion than anion self-diffusion through the chalcogenide shell. On the other hand, urchin-like particles result from the oxidation of Cd, indicating faster oxygen diffusion than cadmium diffusion through the CdO grain boundaries. Because of the dissimilar temperature ranges considered and the polycrystalline nature of the composite shells consistently formed, it is evidenced that the particle geometries obtained from the reaction of Cd particles with chalcogens cannot be predicted from the straightforward extrapolations of the bulk self-diffusion coefficients previously reported.

The modulation of the crystallite nucleation rate versus growth rate allows some extent of tuning over the crystallographic domain size. Such modulation can be achieved either by modifying the precursor concentration or its reactivity, which control the reaction rate. In the sulfidation of Cd particles, when reducing the reaction rate, either by decreasing the concentration of molecular sulfur dissolved in DCB or employing the less-reactive TOPS, a promotion of the crystal growth over nucleation was obtained and CdS shells with larger crystallographic domains were produced. Such an increase of the crystallographic domains was consistently correlated with a variation of the inner radius-to-outer-radius ratio. This experimental evidence can be explained by a shift from a diffusion-limited regime to a reaction-limited shell growth regime. In a reaction-limited growth regime, the low reaction rate allows a homogeneous distribution of the anion across the shell, habilitating the Cd−S reaction to occur at both interfaces simultaneously. More-reactive precursors prevent falling into the reaction-rate-limited regime, but complicate the control of the nucleation/growth rate and may result in relatively porous shells. Such was the case of the reaction of Cd particles with TOPTe to form CdTe.

Post-synthesis processes, to some extent, can solve the intrinsic limitations of the Kirkendall synthetic route on the range of shell thicknesses and crystallographic domain sized potentially obtained. It has been experimentally shown how an annealing process is able to double the crystallographic domain size in CdS shells. However, the stresses resulting from the grain growth eventually lead to the shell rupture. This fact limits the temperature and time ranges for thermal shell sintering and, therefore, the range of shell crystallinity obtained by this procedure. The annealing studies performed also demonstrated that the hollow particles studied here are sufficiently thermally stable for applications at low and moderate temperatures.

Finally, it has been shown how a chemical etching process allows modification of the shell thickness with considerable control in a fast and simple way. A 6-fold reduction of the shell thickness was accomplished, with the heterogeneity of the initial shell thickness being the limiting parameter, limiting the thinnest complete hollow particle that could be obtained.

## AUTHOR INFORMATION

**Corresponding Author**
*E-mail: acabot@irec.cat.

## ACKNOWLEDGMENT

The authors gratefully acknowledge Prof. A. P. Alivisatos and his group for their valuable collaboration. This work was supported by the Spanish MICINN Projects MAT2008-05779, MAT2008-03400-E/MAT and ENE2008-03277-E/CON

## REFERENCES

(1) Yin, Y.; Rioux, R. M.; Erdonmez, C. K.; Hughes, S.; Somorjai, G. A.; Alivisatos, A. P. *Science* **2004**, *304*, 711.

(2) (a) Kim, S.-W.; Kim, M.; Lee, W. Y.; Hyeon, T. *J. Am. Chem. Soc.* **2002**, *124*, 7642. (b) Mitchell, D. T.; Lee, S. B.; Trofin, L.; Li, N.; Nevanen, T. K.; Söderlund, H.; Martin, C. R. *J. Am. Chem. Soc.* **2002**, *124*, 11864. (c) Marinakos, S. M.; Anderson, M. F.; Ryan, J. A.; Martin, L. D.; Feldheim, D. L. *J. Phys. Chem. B* **2001**, *105*, 8872. (d) Gao, J.; Liang, G.; Zhang, B.; Kuang, Y.; Zhang, X. X.; Xu, B. *J. Am. Chem. Soc.* **2007**, *129*, 1428.

(3) Shan, Z. W.; Adesso, G.; Cabot, A.; Sherburne, M. P.; Syed Asif, S. A.; Warren, O. L.; Chrzan, D. C.; Minor, A. M.; Alivisatos, A. P. *Nat. Mater.* **2008**, *7*, 947.

(4) Rapoport, L.; Bilik, Y.; Feldman, Y.; Homyonfer, M.; Cohen, S. R.; Tenne, R. *Nature* **1997**, *387*, 791.

(5) (a) Goll, D.; Berkowitz, A. E.; Bertram, H. N. *Phys. Rev. B* **2004**, *70*, 184432. (b) Rengarajan, R.; Jiang, P.; Colvin, V.; Mittleman, D. *Appl. Phys. Lett.* **2000**, *77*, 3517. (c) Oldenburg, S. J.; Averitt, R. D.; Westcott, S. L.; Halas, N. J. *Chem. Phys. Lett.* **1998**, *288*, 243. (d) Chen, J.; Saeki, F.; Wiley, B. J.; Cang, H.; Cobb, M. J.; Li, Z.-Y.; Au, L.; Zhang, H.; Kimmey, M. B.; Li, X.; Xia, Y. *Nano Lett.* **2005**, *5*, 473.

(6) Cabot, A.; Alivisatos, A. P.; Puntes, V. F.; Balcells, L.; Iglesias, O.; Labarta, A. *Phys. Rev. B* **2009**, *79*, 094419.

(7) Vasquez, Y.; Sra, A. K.; Schaak, R. E. *J. Am. Chem. Soc.* **2005**, *124*, 12504.

(8) Yin, Y.; Erdonmez, C. K.; Cabot, A.; Hughes, S.; Alivisatos, A. P. *Adv. Funct. Mater.* **2006**, *16*, 1389.

(9) (a) Fan, H. J.; Gösele, U.; Zacharias, M. *Small* **2007**, *3*, 1660. (b) Cabot, A.; Puntes, V. F.; Shevchenko, E.; Yin, Y.; Balcells, L.; Marcus, M. A.; Hughes, S. M.; Alivisatos, A. P. *J. Am. Chem. Soc.* **2007**, *129*, 10358. (c) Liu, B.; Zeng, H. C. *J. Am. Chem. Soc.* **2004**, *126*, 16744. (d) Chiang, R.-K.; Chiang, R.-T. *Inorg. Chem.* **2007**, *46*, 369. (e) Railsback, J. G.; Johnston-Peck, A. C.; Wang, J.; Tracy, J. B. *ACS Nano* **2010**, *4*, 1913.

(10) (a) Britt, J.; Ferekides, C. *Appl. Phys. Lett.* **1993**, *62*, 2851. (b) Bruchez, M., Jr.; Moronne, M.; Gin, P.; Weiss, S.; Alivisatos, A. P. *Science* **1998**, *281*, 2013. (c) Li, L.-S.; Alivisatos, A. P. *Adv. Mater.* **2003**, *15*, 408. (d) Hutson, A. R. *Phys. Rev. Lett.* **1960**, *4*, 505. (e) Hutson, A. R.; McFee, J. H.; White, D. L. *Phys. Rev. Lett.* **1961**, *7*, 237.

(11) Cabot, A.; Smith, R. K.; Yin, Y.; Zheng, H.; Reinhard, B. M.; Liu, H.; Alivisatos, A. P. *ACS Nano* **2008**, *2*, 1452.

(12) Wang, Y. L.; Xia, Y. N. *Nano Lett.* **2004**, *4*, 2047.

(13) Dutt, M. B.; Sharma, B. L. *Diffusion in Compound Semiconductors*; Landolt−Börnstein, Group III, Vol. 33A; Springer−Verlag: Berlin, Germany, 1998; Ch. 3.

(14) (a) Whelan, R. C.; Shaw, D. *II−VI Semiconducting Compounds*; Thomas, D. G., Ed.; W. A. Benjamin: New York, 1967; p 451. (b) Borsenberger, P. M.; Stevenson, D. A. *J. Phys. Chem. Solids* **1968**, *29*, 1277. (c) Babentsov, V. N.; Kletskii, S. V.; Tarbaev, N. V. *Semiconductors* **1994**, *28*, 1194.

(15) Woodbury, H. H. *Physics and Chemistry of II−VI Compounds*; Aven, M., Prener, J. S., Eds.; Noord−Hollandsche: Amsterdam, 1967; pp 223−264.

(16) (a) Zmija, J. *Acta Phys. Pol., A* **1973**, *43*, 345. (b) Borsenberger, P. M.; Stevenson, D. A.; Burmeister, R. A. *II−VI Semiconducting Compounds*; Thomas, D. G., Ed.; W. A. Benjamin: New York, 1967; p 439. (c) Dmitrieva, N. V.; Vanyukov, A. V.; Yakovlev, S. G. *Elektron. Tekh. Nauk-Tekh. Sb. Mater.* **1970**, *5*, 150.

(17) (a) Woodbury, H. H. *Phys. Rev. A* **1964**, *134*, 492. (b) Shawn, D. *J. Phys. C: Solid State Phys.* **1984**, *17*, 4759. (c) Jones, E. D. *J. Phys. Chem. Solids* **1972**, *33*, 2063. (d) Sysoev, L. A.; Gelfman, A. J.; Kovaleva, A. D.; Kravchenko, N. G. *Izv. Akad. Nauk SSSR Neorg. Mater.* **1969**, *5*, 2208.

(18) Kumar, V.; Kröger, F. A. *J. Solid State Chem.* **1971**, *3*, 387.

(19) Harrop, P. J. *J. Mater. Sci.* **1968**, *3*, 206.

(20) Haul, R.; Just, D. *J. Appl. Phys.* **1962**, *33*, 487.

(21) Fan, H. J.; Knez, M.; Scholz, R.; Nielsch, K.; Pippel, E.; Hesse, D.; Zacharias, M.; Gösele, U. *Nat. Mater.* **2006**, *5*, 627.

(22) Cabot, A.; Ibañez, M.; Guardia, P.; Hughes, S. M.; Alivisatos, A. P. *J. Am. Chem. Soc.* **2009**, *131*, 11326.

(23) Shaw, D. *J. Phys. C: Solid State Phys.* **1984**, *17*, 4759.

(24) (a) Gusak, A. M.; Zaporozhets, T. V.; Tu, K. N.; Gösele, U. *Philos. Mag.* **2005**, *85*, 4445. (b) Tu, K. N.; Gösele, U. *Appl. Phys. Lett.* **2005**, *86*, 093111.

(25) (a) Glodán, G.; Cserháti, C.; Beszeda, I.; Bekel, D. L. *Appl. Phys. Lett.* **2010**, *97*, 113109. (b) Nakamura, R.; Tokozakura, D.; Lee, J.-G.; Mori, H.; Nakajima, H. *Acta Mater.* **2008**, *56*, 5276.